


Twist-angle dependence of the proximity spin-orbit coupling in graphene on transition-metal dichalcogenides

Yang Li

Department of Physics, Tohoku University, Sendai 980-8578, Japan

Mikito Koshino

Department of Physics, Osaka University, Osaka 560-0043, Japan

 (Received 23 January 2019; revised manuscript received 13 February 2019; published 28 February 2019)

We theoretically study the proximity spin-orbit coupling (SOC) in graphene on a transition-metal dichalcogenides (TMDC) monolayer stacked with arbitrary twist angles. We find that the relative rotation greatly enhances the spin splitting of graphene, typically by a few to ten times compared to the nonrotated geometry, and the maximum splitting is achieved around 20° . The induced SOC can be changed from the Zeeman type to the Rashba type by rotation. The spin splitting is also quite sensitive to the gate-induced potential, and it sharply rises when the graphene's Dirac point is shifted toward the TMDC band. The theoretical method does not need the exact lattice matching and it is applicable to any incommensurate bilayer systems. It is useful for the twist-angle engineering of a variety of van der Waals proximity effects.

DOI: [10.1103/PhysRevB.99.075438](https://doi.org/10.1103/PhysRevB.99.075438)

I. INTRODUCTION

The physical properties of two-dimensional (2D) materials are generally sensitive to the interference with other materials placed in contact. In recent years, a great deal of experimental and theoretical efforts have been made to explore the proximity-induced phenomena in van der Waals heterostructures consisting of different 2D crystals [1]. In particular, it was shown that the negligibly small spin-orbit coupling (SOC) of intrinsic graphene can be significantly enhanced by superimposing on the surface of transition-metal dichalcogenides (TMDC) [2–11], and it is expected to be useful to realize spintronic manipulation in graphene.

In the studies on the proximity effect on 2D materials, however, the importance of the relative lattice orientation has often been overlooked. The previous theoretical calculations of proximity spin-orbit effects of the graphene/TMDC system are limited to the nonrotated geometry [3–6,12]. On the other hand, the sensitive dependence on the relative twist-angle θ was noticed in various 2D heterostructures, and controlling θ is expected to be powerful means of manipulating their electronic properties [13,14]. In graphene on a hexagonal BN system, for instance, the moiré interference pattern gives rise to the formation of the secondary Dirac points and the miniband structure [15–23]. The twisted bilayer graphene also exhibits the dramatic angle-dependent phenomena, such as the flat band formation [24–31] and the emergent superconductivity [32,33]. For a graphene/TMDC heterostructure, the twist-angle dependent band structure was theoretically simulated for several commensurate angles by the density functional theory (DFT) [34–36], and it is also experimentally probed [37–40]. However, the θ dependence of spin-orbit coupling induced on graphene remains still unclear. The twist-angle dependence of SOC was studied for the graphene/topological insulator heterostructures, where the commensurate structures

of $\theta = 0^\circ$ and 30° are compared [41]. It is generally hard to consider arbitrary twist angles in the DFT calculation, because it requires exact lattice matching to have a finite unit cell.

In this paper we theoretically study the proximity SOC effect in graphene-TMDC heterostructures with arbitrary twist-angles θ , and reveal the angle dependence of SOC for various different TMDCs. Using the tight-binding model and the perturbational approach, which do not need the commensurate lattice matching, we obtain the effective Hamiltonian of graphene as a continuous function of θ . We find that the relative rotation greatly enhances the spin splitting, typically by a few to ten times compared to the nonrotated geometry ($\theta = 0$). The maximum splitting is achieved around $\theta \sim 20^\circ$, where the graphene's Dirac cone is strongly hybridized with Q valley of TMDC. We also show that the induced SOC is composed of the Zeeman-like term and the rotated Rashba-like term, and the relative magnitude can be controlled by rotation. Finally, we demonstrate that the spin splitting is quite sensitive to the relative band energy between graphene and TMDC, and it sharply rises when the graphene's Dirac point is shifted toward the TMDC band by applying the gate voltage. The theoretical method proposed here is applicable to any incommensurate bilayer systems where the DFT calculation cannot be used, and therefore it considerably extends the applicability of the theoretical framework to a wide variety of van der Waals heterostructures.

II. THEORETICAL METHODS

A. Lattice structure and the Bloch basis

We consider monolayer graphene placed on the top of a TMDC monolayer. Graphene and TMDC are two-dimensional honeycomb lattices with different lattice periods, $a_G = 2.46 \text{ \AA}$ for graphene and a_T for TMDC given in Table I.

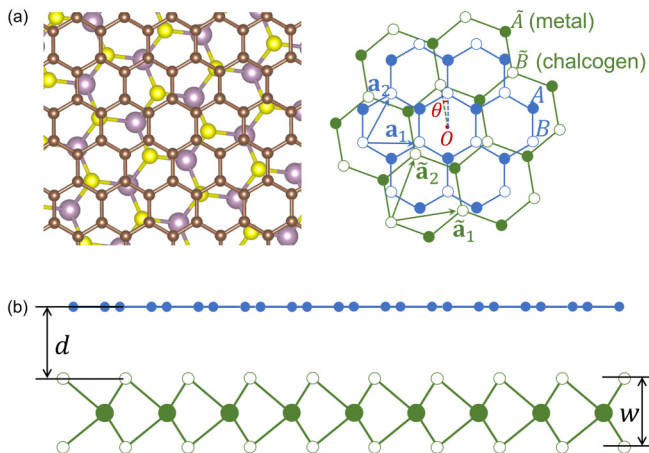
TABLE I. List of parameters for TMDCs and graphene-TMDC bilayers used in this work (see the text).

	MoS ₂	MoSe ₂	WS ₂	WSe ₂
a_T (Å)	3.18 [42]	3.32 [42]	3.18 [42]	3.32 [42]
w (Å)	3.13 [42]	3.34 [42]	3.14 [42]	3.35 [42]
d (Å)	3.37 [42]	3.41 [43]	3.41 [3]	3.42 [3]
$E_T - E_G$ (eV)	0.02 [4]	0.6 [43]	0.12 [3]	1.06 [3,44]

We define the stacking geometry starting from a nonrotated arrangement with parallel bond directions, and then rotating TMDC by the twist-angle θ around the common center of hexagon as in Fig. 1(a). The lattice structure has the C_3 (120°) rotational symmetry with respect to the rotation center. We neglect the degree of freedom of the in-plane parallel translation between TMDC and graphene, since in an incommensurate system it can always be incorporated with the shift of the origin [45].

The lattice vectors of graphene are then given by $\mathbf{a}_1 = a_G(1, 0)$ and $\mathbf{a}_2 = a_G(1/2, \sqrt{3}/2)$, and those of TMDC are by $\tilde{\mathbf{a}}_1 = Ra_T(1, 0)$ and $\tilde{\mathbf{a}}_2 = Ra_T(1/2, \sqrt{3}/2)$, where $R = R(\theta)$ is the rotation matrix. The unit cell area is $S = |\mathbf{a}_1 \times \mathbf{a}_2|$ and $\tilde{S} = |\tilde{\mathbf{a}}_1 \times \tilde{\mathbf{a}}_2|$ for graphene and TMDC, respectively. The reciprocal lattice vectors $\mathbf{a}_1^*, \mathbf{a}_2^*, \tilde{\mathbf{a}}_1^*, \tilde{\mathbf{a}}_2^*$ are defined by $\mathbf{a}_i \cdot \mathbf{a}_j^* = \tilde{\mathbf{a}}_i \cdot \tilde{\mathbf{a}}_j^* = 2\pi\delta_{ij}$. We define d as the distance between the graphene layer and the top chalcogen layer, and w as the distance between top and bottom chalcogen layers. The values of d and w depend on TMDCs as shown in Table I.

We model graphene by the tight-binding model of carbon p_z orbitals, where the sublattice is labeled as $X = p_z^A, p_z^B$ for A and B sites, respectively. For TMDC, we adopt the tight-binding model including three p orbitals for a chalcogen atom and five d orbitals for a transition-metal atom [42]. The orbitals in a TMDC unit cell is labeled by $\tilde{X} = d_{z^2}, d_{xy}, d_{x^2-y^2}, d_{xz}, d_{yz}, p_x^t, p_y^t, p_z^t, p_x^b, p_y^b, p_z^b$, where t and b represent top and bottom chalcogen layers. The positions of


 FIG. 1. (a) Top view and (b) the side view of graphene on TMDC monolayer with twist-angle θ .

the orbitals are given by

$$\begin{aligned} \mathbf{R}_X &= n_1 \mathbf{a}_1 + n_2 \mathbf{a}_2 + \boldsymbol{\tau}_X \quad (\text{graphene}), \\ \mathbf{R}_{\tilde{X}} &= \tilde{n}_1 \tilde{\mathbf{a}}_1 + \tilde{n}_2 \tilde{\mathbf{a}}_2 + \boldsymbol{\tau}_{\tilde{X}} \quad (\text{TMDC}), \end{aligned} \quad (1)$$

where n_i and \tilde{n}_i are integers, and $\boldsymbol{\tau}_X$ and $\boldsymbol{\tau}_{\tilde{X}}$ are the sublattice position inside the unit cell. Specifically, they are expressed as $\boldsymbol{\tau}_{p_z^A} = -\boldsymbol{\tau}_1$, $\boldsymbol{\tau}_{p_z^B} = \boldsymbol{\tau}_1$ for graphene, and $\boldsymbol{\tau}_{\tilde{X}} = -\tilde{\boldsymbol{\tau}}_1 - (d + w/2)\mathbf{e}_z$ for the transition-metal d orbitals and $\boldsymbol{\tau}_{\tilde{X}} = \tilde{\boldsymbol{\tau}}_1 - d\mathbf{e}_z$, $\tilde{\boldsymbol{\tau}}_1 - (d + w)\mathbf{e}_z$ for the top and bottom chalcogen p orbitals, respectively, where $\boldsymbol{\tau}_1 = (-\mathbf{a}_1 + 2\mathbf{a}_2)/3$ and $\tilde{\boldsymbol{\tau}}_1 = (-\tilde{\mathbf{a}}_1 + 2\tilde{\mathbf{a}}_2)/3$.

The Hamiltonian is spanned by the Bloch bases,

$$\begin{aligned} | \mathbf{k}, X, s \rangle &= \frac{1}{\sqrt{N}} \sum_{\mathbf{R}_X} e^{i\mathbf{k} \cdot \mathbf{R}_X} | \mathbf{R}_X, s \rangle \quad (\text{graphene}), \\ | \tilde{\mathbf{k}}, \tilde{X}, \tilde{s} \rangle &= \frac{1}{\sqrt{\tilde{N}}} \sum_{\mathbf{R}_{\tilde{X}}} e^{i\tilde{\mathbf{k}} \cdot \mathbf{R}_{\tilde{X}}} | \mathbf{R}_{\tilde{X}}, \tilde{s} \rangle \quad (\text{TMDC}), \end{aligned} \quad (2)$$

where s, \tilde{s} are the spin indexes, \mathbf{k} and $\tilde{\mathbf{k}}$ are the two-dimensional Bloch wave vectors parallel to the layer, and $N = S_{\text{tot}}/S$ and $\tilde{N} = S_{\text{tot}}/\tilde{S}$ are the number of unit cells of TMDC and graphene, respectively, in the total system area S_{tot} .

B. Tight-binding Hamiltonian

The total tight-binding Hamiltonian is expressed as $H = H_G + H_T + H_{\text{int}}$, where H_G and H_T are the Hamiltonian for the intrinsic graphene monolayer and TMDC monolayer, respectively, and H_{int} is for the coupling between graphene and TMDC. For H_G , we use the standard tight-binding model of carbon p_z orbitals [46,47]. For H_T , we adopt the hopping parameters based on the first-principles calculation [42] where the spin-orbit coupling is included by the on-site $\mathbf{L} \cdot \mathbf{S}$ term for each atom. The on-site energy of the TMDC atoms relative to the carbon atoms is extracted from the relative energy $E_T - E_G$ from the graphene Dirac point to TMDC conduction band edges in the first-principles calculations [3,4,40,43,44], which are listed in Table I.

For the interlayer interaction H_{int} , we assume that the transfer integral from \mathbf{R}_X to $\mathbf{R}_{\tilde{X}}$ is expressed as $-T_{\tilde{X}X}(\mathbf{R}_{\tilde{X}} - \mathbf{R}_X)$, with the standard Slater-Koster parametrization [48] and the exponential decay in the distance. Specifically, the transfer integrals from a graphene's p_z orbital to TMDC's p and d orbitals are given by

$$\begin{aligned} -T_{p_x, p_z}(\mathbf{R}) &= e_x e_z V_{pp\sigma} - e_x e_z V_{pp\pi}, \\ -T_{p_y, p_z}(\mathbf{R}) &= e_y e_z V_{pp\sigma} - e_y e_z V_{pp\pi}, \\ -T_{p_z, p_z}(\mathbf{R}) &= e_z^2 V_{pp\sigma} + (1 - e_z^2) V_{pp\pi}, \\ -T_{d_{xz}, p_z}(\mathbf{R}) &= \sqrt{3} e_z^2 e_x V_{pd\sigma} + e_x (1 - 2e_z^2) V_{pd\pi}, \\ -T_{d_{yz}, p_z}(\mathbf{R}) &= \sqrt{3} e_z^2 e_y V_{pd\sigma} + e_y (1 - 2e_z^2) V_{pd\pi}, \\ -T_{d_{xy}, p_z}(\mathbf{R}) &= \sqrt{3} e_x e_y e_z V_{pd\sigma} - 2e_x e_y e_z V_{pd\pi}, \\ -T_{d_{x^2-y^2}, p_z}(\mathbf{R}) &= \frac{\sqrt{3}}{2} e_z (e_x^2 - e_y^2) V_{pd\sigma} - e_z (e_x^2 - e_y^2) V_{pd\pi}, \end{aligned}$$

$$\begin{aligned}
 -T_{d_{3z^2-r^2}p_z}(\mathbf{R}) = & e_z[e_z^2 - (e_x^2 + e_y^2)/2]V_{pd\sigma} \\
 & + \sqrt{3}e_z(e_x^2 + e_y^2)V_{pd\pi}, \quad (3)
 \end{aligned}$$

where $-T_{ab}(\mathbf{R})$ stands for the transfer integral from the orbital b at the origin to the orbital a at the position \mathbf{R} , and $e_i = R_i/R$ ($i = x, y, z$). $V_{p\alpha\beta}(\mathbf{R})$ is the transfer integral between carbon p orbital and a ($= p, d$) orbital of TMDC, arranged in β ($= \sigma, \pi$) configuration. Here we assume exponentially decaying functions [26,49,50]

$$\begin{aligned}
 V_{pp\beta}(\mathbf{R}) &= V_{pp\beta}^0 e^{-(R-d_{C-Ch})/r_{C-Ch}^0}, \\
 V_{pd\beta}(\mathbf{R}) &= V_{pd\beta}^0 e^{-(R-d_{C-M})/r_{C-M}^0}. \quad (4)
 \end{aligned}$$

Here d_{C-Ch} (d_{C-M}) is the reference bond length of a carbon and chalcogen (transition-metal) atom, and the r_{C-Ch}^0 (r_{C-M}^0) is the characteristic decay length in the hopping amplitude. The prefactors $V_{pp\sigma}^0$ and $V_{pp\pi}^0$ are the hopping integrals at the reference bond lengths, which are given by the Harrison's model [51]

$$\begin{aligned}
 V_{pp\sigma}^0 &= 2.22\eta_{C-Ch} \frac{\hbar^2}{md_{C-Ch}^2}, \\
 V_{pp\pi}^0 &= -0.63\eta_{C-Ch} \frac{\hbar^2}{md_{C-Ch}^2}, \\
 V_{pd\sigma}^0 &= -\frac{3\sqrt{15}}{2\pi} \eta_{C-M} \frac{\hbar^2 \sqrt{r_p r_d^3}}{md_{C-M}^2}, \\
 V_{pd\pi}^0 &= -\frac{3\sqrt{5}}{2\pi} \eta_{C-M} \frac{\hbar^2 \sqrt{r_p r_d^3}}{md_{C-M}^2}. \quad (5)
 \end{aligned}$$

Here m is the bare electron mass, r_p and r_d are the radii of p orbital and d orbitals, respectively, and η_{C-Ch} and η_{C-M} are the fitting parameters ($\eta_{C-Ch} = \eta_{C-M} = 1$ in the original model [51]). We adopt the parameters $d_{C-S} = 1.82 \text{ \AA}$ [52], $d_{C-Se} = 1.94 \text{ \AA}$ [53], $d_{C-Mo} = 2.059 \text{ \AA}$ [54], and $d_{C-W} = 2.2 \text{ \AA}$ [55], $r_p = 6.59 \text{ \AA}$ for C, and $r_d = 1.231$ and 1.268 \AA for Mo and W, respectively [51]. The decaying length r_{C-X}^0 and the amplitude parameter η_{C-X} are tuned to reproduce the first-principles band structures for MoS₂ and WS₂ at 0° rotation. Obtained values are $r_{C-S}^0 = 1.131 \text{ \AA}$, $r_{C-Se}^0 = 1.205 \text{ \AA}$, $r_{C-Mo}^0 = 1.280 \text{ \AA}$, $r_{C-W}^0 = 1.367 \text{ \AA}$, and $\eta_{C-S} = 1.26$, $\eta_{C-Mo} = 0.92$, $\eta_{C-W} = 0.30$, which are used throughout the paper.

C. Effective low-energy Hamiltonian with proximity SOC effect

Below we derive the low-energy effective Hamiltonian of graphene with TMDC proximity effect using the second order perturbation. The following approach is applicable to any 2D heterostructures in which the interlayer coupling is written in a distant-dependent tight-binding form of $-T_{\tilde{X}X}(\mathbf{R}_{\tilde{X}} - \mathbf{R}_X)$. The coupling between the Bloch states of graphene and that of TMDC is given by [29,45]

$$\begin{aligned}
 & \langle \tilde{\mathbf{k}}, \tilde{X}, \tilde{s} | H_{\text{int}} | \mathbf{k}, X, s \rangle \\
 &= - \sum_{\mathbf{G}, \tilde{\mathbf{G}}} t_{\tilde{X}X}(\mathbf{k} + \mathbf{G}) e^{-i\mathbf{G} \cdot \boldsymbol{\tau}_X + i\tilde{\mathbf{G}} \cdot \boldsymbol{\tau}_{\tilde{X}}} \delta_{\mathbf{k}+\mathbf{G}, \tilde{\mathbf{k}}+\tilde{\mathbf{G}}} \delta_{s\tilde{s}}. \quad (6)
 \end{aligned}$$

Here $\mathbf{G} = m_1 \mathbf{a}_1^* + m_2 \mathbf{a}_2^*$ and $\tilde{\mathbf{G}} = \tilde{m}_1 \tilde{\mathbf{a}}_1^* + \tilde{m}_2 \tilde{\mathbf{a}}_2^*$ are reciprocal lattice vectors of graphene and TMDC, respectively, $t_{\tilde{X}X}(\mathbf{q})$ is the in-plane Fourier transform of the transfer integral defined by

$$t_{\tilde{X}X}(\mathbf{q}) = \frac{1}{\sqrt{SS}} \int T_{\tilde{X}X}(\mathbf{r} + z_{\tilde{X}X} \mathbf{e}_z) e^{-i\mathbf{q} \cdot \mathbf{r}} d^2 r, \quad (7)$$

where $z_{\tilde{X}X} = (\boldsymbol{\tau}_{\tilde{X}} - \boldsymbol{\tau}_X) \cdot \mathbf{e}_z$.

The Hamiltonian of graphene including the TMDC proximity effect can be obtained by the second order perturbation as $H_{\text{eff}}(\mathbf{k}) = H_G(\mathbf{k}) + V_{\text{eff}}(\mathbf{k})$, where

$$[V_{\text{eff}}(\mathbf{k})]_{X's', Xs} = \sum_{\tilde{n}, \tilde{\mathbf{k}}} \frac{\langle \mathbf{k}, X', s' | H_{\text{int}} | \tilde{n}, \tilde{\mathbf{k}} \rangle \langle \tilde{n}, \tilde{\mathbf{k}} | H_{\text{int}} | \mathbf{k}, X, s \rangle}{E_G - E_{\tilde{n}, \tilde{\mathbf{k}}}}. \quad (8)$$

Here E_G is the energy of the graphene's Dirac point, and $E_{\tilde{n}, \tilde{\mathbf{k}}}$ and $|\tilde{n}, \tilde{\mathbf{k}}\rangle$ are the eigenenergy and eigenstate of H_T , respectively, with the band index \tilde{n} (including the spin degree of freedom) and the Bloch vector $\tilde{\mathbf{k}}$. Note that $|\tilde{n}, \tilde{\mathbf{k}}\rangle$ is written as a linear combination of $|\tilde{\mathbf{k}}, \tilde{X}, \tilde{s}\rangle$ of the same $\tilde{\mathbf{k}}$. The summation over $\tilde{\mathbf{k}}$ in Eq. (8) is taken according to the condition Eq. (6).

The low-energy Hamiltonian is obtained by expanding $H_{\text{eff}}(\mathbf{k})$ around the valley center $\mathbf{K}_\xi \equiv -\xi(2\mathbf{a}_1^* + \mathbf{a}_2^*)/3$, where $\xi = \pm 1$ is the valley index. Within the linear term, H_G is approximated by $H_G^{(\xi)}(\mathbf{k}) = -\hbar v(\mathbf{k} - \mathbf{K}_\xi) \cdot (\xi\sigma_x, \sigma_y)$, where v is the band velocity of graphene, and σ_x and σ_y are Pauli matrices for the sublattice space $X = p_z^A, p_z^B$ [46,47]. For the proximity SOC term, we only take the zeroth order $V_{\text{eff}}(\mathbf{K}_\xi) \equiv V_{\text{eff}}^{(\xi)}$. Now that the transfer integral $T_{\tilde{X}X}(\mathbf{R})$ attenuates exponentially and so does its Fourier transform $t_{\tilde{X}X}(\mathbf{q})$, it suffices to keep only a few $\tilde{\mathbf{k}}$'s in the summation of Eq. (8). For $\mathbf{k} = \mathbf{K}_\xi$, the dominant contribution comes from three points, $\tilde{\mathbf{k}} = \mathbf{K}_\xi + \xi \tilde{\mathbf{a}}_1^*$, $\mathbf{K}_\xi + \xi(\mathbf{a}_1^* + \tilde{\mathbf{a}}_2^*)$, $\mathbf{K}_\xi + \xi(\mathbf{a}_1^* + \mathbf{a}_2^* - \tilde{\mathbf{a}}_1^* - \tilde{\mathbf{a}}_2^*)$, while the effect of other $\tilde{\mathbf{k}}$'s are negligibly small. In this way, the effective proximity potential can be obtained by considering TMDC Bloch states at only three wave points, and the corresponding computing cost is considerably low.

We can show that $V_{\text{eff}}^{(\xi)}$ can be written as

$$V_{\text{eff}}^{(\xi)} = \frac{\lambda}{2} \xi s_z + \frac{\lambda_R}{2} e^{-i\phi s_z/2} (\xi \sigma_x s_y - \sigma_y s_x) e^{i\phi s_z/2}, \quad (9)$$

where s_i ($i = x, y, z$) is the Pauli matrix for spin. It is explicitly written in a matrix form,

$$\begin{aligned}
 V_{\text{eff}}^{(+)} &= \begin{pmatrix} \lambda/2 & & & \\ & \lambda/2 & -i\lambda_R e^{-i\phi} & \\ & i\lambda_R e^{i\phi} & -\lambda/2 & \\ & & & -\lambda/2 \end{pmatrix}, \\
 V_{\text{eff}}^{(-)} &= \begin{pmatrix} -\lambda/2 & & & \\ & -\lambda/2 & & i\lambda_R e^{-i\phi} \\ & & \lambda/2 & \\ -i\lambda_R e^{i\phi} & & & \lambda/2 \end{pmatrix}, \quad (10)
 \end{aligned}$$

where the bases are arranged by order of $(X, s) = (A, \uparrow)$, (B, \uparrow) , (A, \downarrow) , and (B, \downarrow) . The difference in the diagonal elements λ leads to the spin splitting between spin up and spin down, and the off-diagonal term λ_R mixes the different spins. The term with λ_R is similar to the Rashba spin-orbit coupling

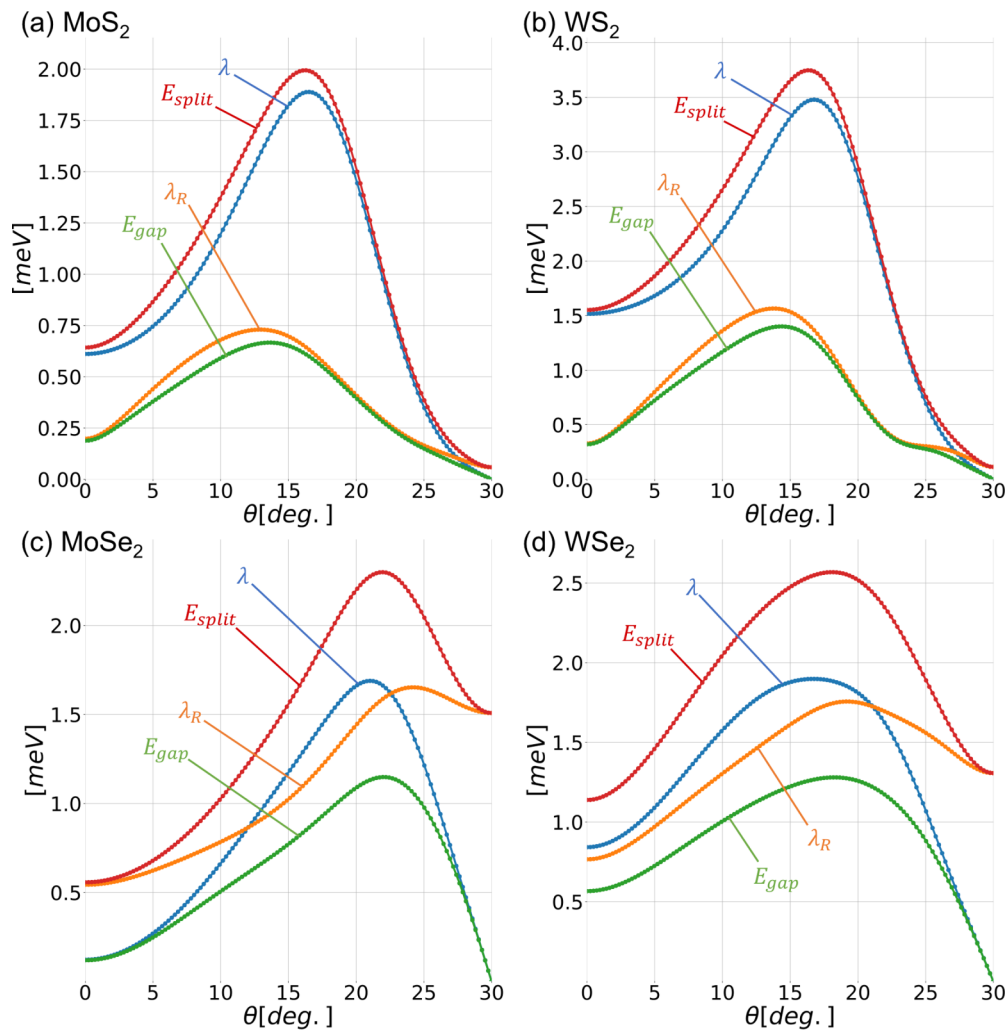


FIG. 2. Spin-orbit parameters λ , λ_R , the central energy gap E_{gap} , and the spin splitting E_{split} , as a function of the twist-angle θ in graphenes on (a) MoS₂, (b) WS₂, (c) MoSe₂, and (d) WSe₂ monolayer.

[5,56] but here the spin axis can be rotated by an angle ϕ on the xy plane. The energy gap at the charge neutral point is given by $E_{\text{gap}} = |\lambda\lambda_R|/(\lambda^2 + \lambda_R^2)^{1/2}$. The spin splitting width in large k is given by $E_{\text{split}} = (\lambda^2 + \lambda_R^2)^{1/2}$. The effective Hamiltonian $H_{\text{eff}}^{(\xi)} = H_G^{(\xi)}(\mathbf{k}) + V_{\text{eff}}^{(\xi)}$ is formally equivalent with that of the asymmetric bilayer graphene [57,58], where the spin up and down correspond to layer 1 and 2, respectively, and λ_R and λ to the interlayer coupling and the interlayer asymmetric potential, respectively.

The form of Eq. (9) is forced by the symmetry of the system. The terms in Eq. (9) are generally allowed in the time reversal symmetry \mathcal{T} and the C_3 symmetry. Actually, the terms proportional to σ_z (different on-site energies at A and B sites) [5] and $\xi\sigma_z s_z$ (the Kane-Mele term) [56] are also possible under \mathcal{T} and C_3 , but in $V_{\text{eff}}^{(\xi)}$ it is prohibited by the incommensurability between graphene and TMDC, as explained in the Appendix. An additional space symmetry imposes a constraint on $V_{\text{eff}}^{(\xi)}$. At $\theta = 0$, the reflection symmetry $R_x : (x, y, z) \rightarrow (-x, y, z)$ requires $e^{i\phi}$ is real. At $\theta = 30^\circ$, the reflection symmetry $R_y : (x, y, z) \rightarrow (x, -y, z)$ requires real $e^{i\phi}$ and also $\lambda = 0$, i.e., the SOC is dominated by the Rashba

term. The detailed argument of the symmetry consideration is presented in the Appendix.

III. NUMERICAL RESULTS

We numerically calculate $V_{\text{eff}}^{(\xi)}$ for MoS₂, WS₂, MoSe₂, and WSe₂. Figure 2 summarizes the results, where λ , λ_R , the central energy gap E_{gap} , and the spin splitting E_{split} are plotted against the twist-angle θ . In Fig. 3 we present the band structures for each system at the rotation angles $\theta = 0^\circ$, 15° , and 30° . In the band plots of MoS₂ and WS₂ at $\theta = 0^\circ$, the dotted green line indicates the first DFT calculations, from which we extract the interlayer hopping parameters. For the DFT calculation, we assume the approximate commensurate lattice structure of which unit cell is comprised of a 3×3 supercell of MoS₂ and a 4×4 of graphene, and use Quantum Espresso [59,60] with the generalized gradient approximation [61]. We can see that the effective model well reproduces the DFT band structure.

For the angle dependence we find that λ and λ_R are greatly enhanced by rotation, and they take the maximum around

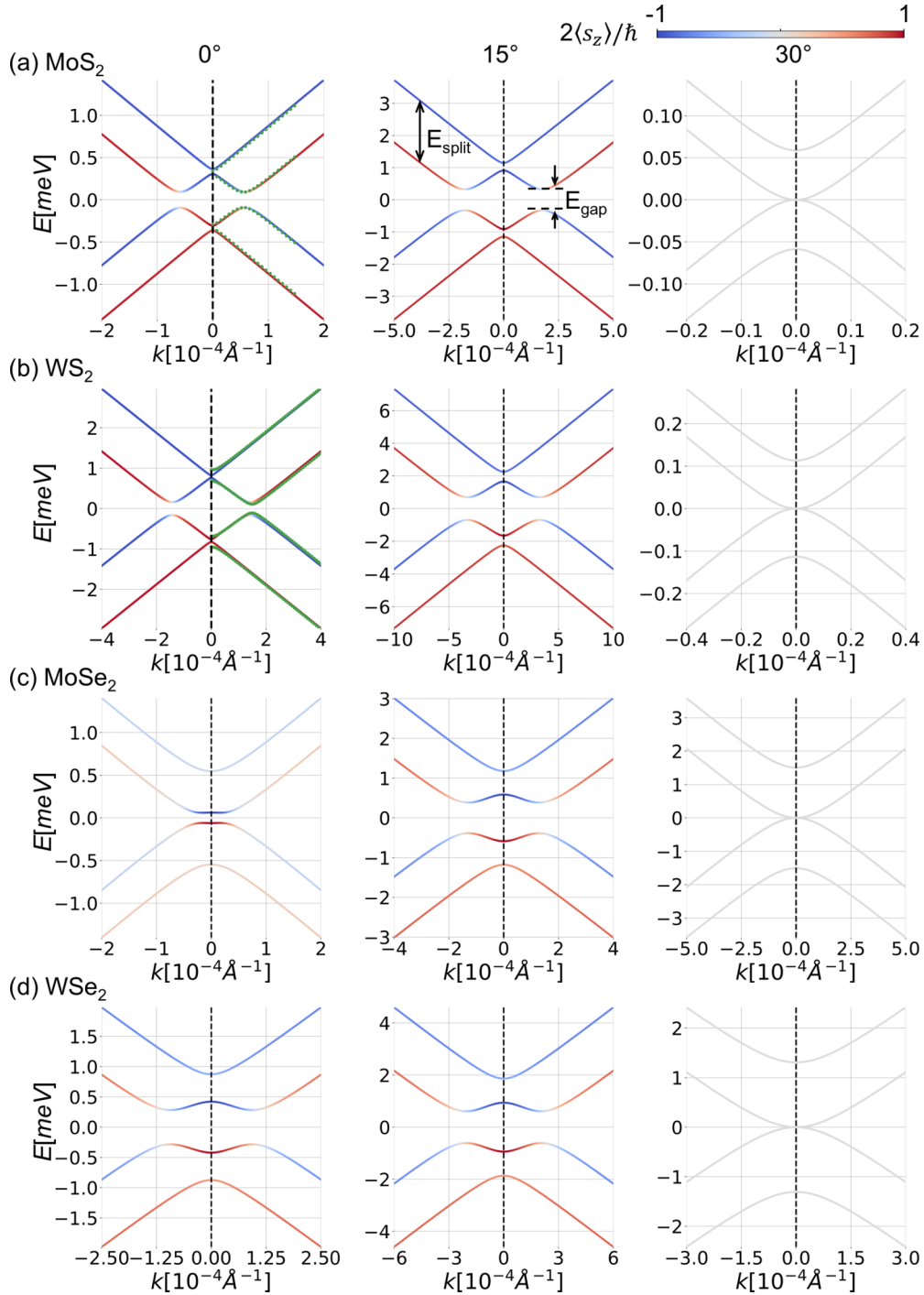


FIG. 3. Band structures for graphene on (a) MoS₂, (b) WS₂, (c) MoSe₂, and (d) WSe₂ monolayer at the twist angles $\theta = 0^\circ, 15^\circ,$ and 30° , where color indicates the expectation value of s_z . In the band plots of MoS₂ and WS₂ at $\theta = 0^\circ$, the dotted green line indicates the DFT calculations.

$\theta \sim 20^\circ$. For WS₂, in particular, the maximum splitting is about 5 times as large as that of 0° . At 30° , the parameter λ vanishes and the V_{eff} is dominated by λ_R as expected. There the band structure is formally equivalent to the symmetric *AB*-stacked bilayer graphene, and the expectation value of spin lies on the *xy* plane.

The enhancement of the spin splitting near 20° can be understood by considering the second order process, Eq. (8). The amplitude of V_{eff} is related to the spin splitting of the

TMDC bands at $\tilde{\mathbf{k}}$ points which are hybridized with the graphene's Dirac point. Figure 4(a) illustrates the positions of the three dominant $\tilde{\mathbf{k}}$'s for $\xi = +$, in WS₂ with $\theta = 0^\circ, 17.9^\circ,$ and 30° . Figure 4(b) presents the band structure of WS₂ with the vertical dashed lines indicating the $\tilde{\mathbf{k}}$'s for the three rotation angles. Now the lowest valence band of TMDC makes the greatest contribution to V_{eff} , as it is the closest to the graphene's Dirac point energy (black horizontal line), leading to a small denominator in Eq. (8). We can see that the $\tilde{\mathbf{k}}$ point

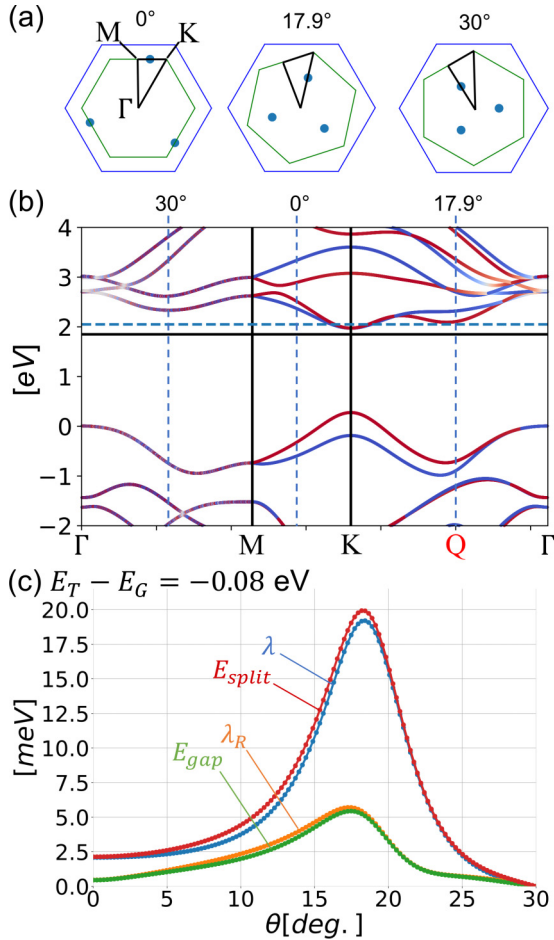


FIG. 4. (Top) Position of three dominant $\bar{\mathbf{k}}$ points for $\xi = +$, in WS₂ with $\theta = 0^\circ$, 17.9° , and 30° . Blue (green) hexagon represents the first Brillouin zone of graphene (WS₂). (Bottom left) Band structure of WS₂, where the vertical dashed lines indicate the $\bar{\mathbf{k}}$ for the three rotation angles, and the black horizontal line is the energy of graphene's Dirac cone without gate voltage. (Bottom right) Plot similar to Fig. 2, calculated for WS₂ with $E_T - E_G = -0.08$ eV, indicated by the blue dashed horizontal line in (b).

for 17.9° happens to be very close to the Q valley, where the magnitude of the spin splitting is much greater than in other angles. This qualitatively explains the sharp rise of λ and λ_R around 20° . Actually, the spin splitting can be even enhanced by shifting the relative energy between graphene and TMDC. Figure 4(c) plots the angle dependence of the spin splitting of WS₂ with $E_T - E_G = -0.08$ eV, where the graphene's Fermi energy (blue horizontal line) hits the bottom of the Q valley. Although the Fermi energy is just a little higher than in Fig. 2(b), the maximum spin splitting sharply increases to 20 meV, about 10 times as big as in $\theta = 0$, because the denominator in Eq. (8) becomes very small. This suggests that tuning of the spin-orbit coupling would be possible using the external gate voltage.

Finally, the graphene under the proximity potential has the nonzero valley Hall conductivity when the Fermi energy lies in the central gap. The Hall conductivity of each valley sector can be calculated using the Berry

curvature as

$$\sigma_{xy}^{(\xi)} = \frac{e^2}{h} \sum_{n \in \text{occ.}} \int \frac{d^2 \mathbf{k}}{2\pi} \nabla_{\mathbf{k}} \times \mathbf{a}_n(\mathbf{k}) = -\frac{e^2}{h} \xi \text{sgn}(\lambda), \quad (11)$$

where $\mathbf{a}_n(\mathbf{k}) = -i \langle u_{n\mathbf{k}} | \nabla_{\mathbf{k}} | u_{n\mathbf{k}} \rangle$ is the Berry connection, $u_{n\mathbf{k}}$ is the Bloch function (eigenvector of $H_{\text{eff}}^{(\xi)}$) of the band n , and occ. stands for the occupied valence bands ($n = 1, 2$). As a result, the valley Hall conductivity becomes $\sigma_{xy}^{(+)} - \sigma_{xy}^{(-)} = -(2e^2/h) \text{sgn}(\lambda)$.

IV. CONCLUSION

To conclude, we have studied the proximity spin-orbit interaction in graphene-TMDC bilayers stacked with arbitrary twist angles. By using the perturbational approach based on the tight-binding model, we derived the effective Hamiltonian of graphene as a continuous function of the twist-angle θ , and found that the magnitude of SOC is greatly enhanced by the rotation. We also show that the SOC sharply rises when the graphene's Dirac point is shifted toward the TMDC band, by applying the gate voltage. The theoretical method proposed here does not need the exact lattice matching, so that it is applicable to any incommensurate bilayer systems which cannot be treated by the DFT calculation. It would be useful for the twist-angle engineering of a wide variety of van der Waals proximity effects, including ferromagnetism and superconductivity.

ACKNOWLEDGMENT

M.K. acknowledges the financial support of JSPS KAKENHI Grant No. JP17K05496.

APPENDIX: SYMMETRY CONSIDERATION OF THE INDUCED EFFECTIVE POTENTIAL ON GRAPHENE

Here we argue about the restriction on the effective spin-orbit Hamiltonian V_{eff}^{\pm} in Eq. (9). Apart from the spin part, the low-energy state of graphene is expressed by [46]

$$|\psi\rangle = \sum_{\xi=\pm} \left[\sum_{\mathbf{R}_A} F_A^{\xi}(\mathbf{R}_A) e^{i\mathbf{K}_{\xi} \cdot \mathbf{R}_A} |\mathbf{R}_A\rangle + \sum_{\mathbf{R}_B} F_B^{\xi}(\mathbf{R}_B) e^{i\mathbf{K}_{\xi} \cdot \mathbf{R}_B} |\mathbf{R}_B\rangle \right], \quad (\text{A1})$$

where \mathbf{R}_X ($X = A, B$) runs over the atomic positions of sublattice X , $|\mathbf{R}_X\rangle$ is the p_z orbital at \mathbf{R}_X , and $F_X^{\xi}(\mathbf{r})$ is the smooth envelop function of sublattice X and the valley ξ . The state is represented by the four-component wave function $\mathbf{F}(\mathbf{r}) = (F_A^+(\mathbf{r}), F_B^+(\mathbf{r}), F_A^-(\mathbf{r}), F_B^-(\mathbf{r}))^T$, where T is the matrix transposition.

The time reversal operation \mathcal{T} is written as

$$\mathcal{T}|\psi\rangle = \sum_{\xi=\pm} \left[\sum_{\mathbf{R}_A} [F_A^{\xi}(\mathbf{R}_A)]^* e^{-i\mathbf{K}_{\xi} \cdot \mathbf{R}_A} |\mathbf{R}_A\rangle + \sum_{\mathbf{R}_B} [F_B^{\xi}(\mathbf{R}_B)]^* e^{-i\mathbf{K}_{\xi} \cdot \mathbf{R}_B} |\mathbf{R}_B\rangle \right]$$

$$\begin{aligned}
 &= \sum_{\xi=\pm} \left[\sum_{\mathbf{R}_A} [F_A^{-\xi}(\mathbf{R}_A)]^* e^{i\mathbf{K}_\xi \cdot \mathbf{R}_A} |\mathbf{R}_A\rangle \right. \\
 &\quad \left. + \sum_{\mathbf{R}_B} [F_B^{-\xi}(\mathbf{R}_B)]^* e^{i\mathbf{K}_\xi \cdot \mathbf{R}_B} |\mathbf{R}_B\rangle \right], \quad (\text{A2})
 \end{aligned}$$

where we used $-\mathbf{K}_\xi = \mathbf{K}_{-\xi}$. In the four-component representation, this is written as

$$\mathcal{T} \begin{pmatrix} F_A^+(\mathbf{r}) \\ F_B^+(\mathbf{r}) \\ F_A^-(\mathbf{r}) \\ F_B^-(\mathbf{r}) \end{pmatrix} = \begin{pmatrix} F_A^-(\mathbf{r}) \\ F_B^-(\mathbf{r}) \\ F_A^+(\mathbf{r}) \\ F_B^+(\mathbf{r}) \end{pmatrix}^*, \quad (\text{A3})$$

or simply expressed as $\mathcal{T}\mathbf{F} = \tau_x \mathcal{K} \mathbf{F}$, where τ_i ($i = x, y, z$) is the Pauli matrices for the valley pseudospin, and \mathcal{K} is a complex conjugate operation. As the time reversal operation for electron spin is given by $is_y K$ with the spin Pauli matrix s_i ($i = x, y, z$), the total time reversal operation including orbital and spin is given by

$$\mathcal{T} = is_y \tau_x \mathcal{K}. \quad (\text{A4})$$

The in-plane 120° rotation operation C_3 is written as

$$\begin{aligned}
 C_3 |\psi\rangle &= \sum_{\xi=\pm} \left[\sum_{\mathbf{R}_A} F_A^\xi(\mathbf{R}_A) e^{i\mathbf{K}_\xi \cdot \mathbf{R}_A} |C_3 \mathbf{R}_A\rangle \right. \\
 &\quad \left. + \sum_{\mathbf{R}_B} F_B^\xi(\mathbf{R}_B) e^{i\mathbf{K}_\xi \cdot \mathbf{R}_B} |C_3 \mathbf{R}_B\rangle \right]. \quad (\text{A5})
 \end{aligned}$$

When the rotation origin is chosen on the center of a hexagon in the honeycomb lattice, C_3 maps a A site to some other A site, and a B site to other B site. By writing $C_3 \mathbf{R}_A = \mathbf{R}'_A$ and $C_3 \mathbf{R}_B = \mathbf{R}'_B$, we have

$$\begin{aligned}
 C_3 |\psi\rangle &= \sum_{\xi=\pm} \left[\sum_{\mathbf{R}'_A} F_A^\xi(C_3^{-1} \mathbf{R}'_A) e^{i\mathbf{K}_\xi \cdot C_3^{-1} \mathbf{R}'_A} |\mathbf{R}'_A\rangle \right. \\
 &\quad \left. + \sum_{\mathbf{R}'_B} F_B^\xi(C_3^{-1} \mathbf{R}'_B) e^{i\mathbf{K}_\xi \cdot C_3^{-1} \mathbf{R}'_B} |\mathbf{R}'_B\rangle \right] \\
 &= \sum_{\xi=\pm} \left[\sum_{\mathbf{R}'_A} \omega^\xi F_A^\xi(C_3^{-1} \mathbf{R}'_A) e^{i\mathbf{K}_\xi \cdot \mathbf{R}'_A} |\mathbf{R}'_A\rangle \right. \\
 &\quad \left. + \sum_{\mathbf{R}'_B} \omega^{-\xi} F_B^\xi(C_3^{-1} \mathbf{R}'_B) e^{i\mathbf{K}_\xi \cdot \mathbf{R}'_B} |\mathbf{R}'_B\rangle \right], \quad (\text{A6})
 \end{aligned}$$

where we used $e^{i\mathbf{K}_\xi \cdot C_3^{-1} \mathbf{R}'_A} = \omega^\xi e^{i\mathbf{K}_\xi \cdot \mathbf{R}'_A}$ and $e^{i\mathbf{K}_\xi \cdot C_3^{-1} \mathbf{R}'_B} = \omega^{-\xi} e^{i\mathbf{K}_\xi \cdot \mathbf{R}'_B}$. In the four-component representation it is written as

$$C_3 \begin{pmatrix} F_A^+(\mathbf{r}) \\ F_B^+(\mathbf{r}) \\ F_A^-(\mathbf{r}) \\ F_B^-(\mathbf{r}) \end{pmatrix} = \begin{pmatrix} \omega F_A^+(C_3^{-1} \mathbf{r}) \\ \omega^{-1} F_B^+(C_3^{-1} \mathbf{r}) \\ \omega^{-1} F_A^-(C_3^{-1} \mathbf{r}) \\ \omega F_B^-(C_3^{-1} \mathbf{r}) \end{pmatrix}. \quad (\text{A7})$$

It is shortened as $C_3 \mathbf{F} = [-(1/2) + i(\sqrt{3}/2)\tau_z \sigma_z] \tilde{C}_3 \mathbf{F}$, where \tilde{C}_3 represents the 120° rotation for the envelop function, i.e., $\tilde{C}_3 \mathbf{F}(\mathbf{r}) = \mathbf{F}(C_3^{-1} \mathbf{r})$, and σ_i ($i = x, y, z$) is the Pauli matrices for A, B sublattice. Since the time reversal operation for electron spin is given by $e^{-i(2\pi/3)s_z/2} = (1/2) - i(\sqrt{3}/2)s_z$, the total time reversal operation including orbital and spin becomes [62]

$$C_3 = \left(\frac{1}{2} - i \frac{\sqrt{3}}{2} s_z \right) \left(-\frac{1}{2} + i \frac{\sqrt{3}}{2} \tau_z \sigma_z \right) \tilde{C}_3. \quad (\text{A8})$$

The spin-orbit interaction V_{eff} [Eq. (9)] is written as

$$\begin{aligned}
 V_{\text{eff}} &= \frac{\lambda}{2} \tau_z s_z + \frac{\lambda_R}{2} e^{-i\phi s_z/2} (\tau_z \sigma_x s_y - \sigma_y s_x) e^{i\phi s_z/2} \\
 &= \frac{\lambda}{2} \tau_z s_z + \frac{\lambda_R}{2} [\cos \phi (\tau_z \sigma_x s_y - \sigma_y s_x) \\
 &\quad - \sin \phi (\tau_z \sigma_x s_x + \sigma_y s_y)], \quad (\text{A9})
 \end{aligned}$$

where the valley index ξ is replaced with the Pauli matrix τ_z . Then it is straightforward to check that V_{eff} commutes with \mathcal{T} and C_3 . An additional space symmetry imposes a constraint on V_{eff} . At $\theta = 0$, the reflection symmetry $R_x : (x, y, z) \rightarrow (-x, y, z)$ requires $e^{i\phi}$ is real. At $\theta = 30^\circ$, the reflection symmetry $R_y : (x, y, z) \rightarrow (x, -y, z)$ requires real $e^{i\phi}$ and also $\lambda = 0$, i.e., the SOC is dominated by the Rashba term. This can be proved by noting that R_x and R_y are written as

$$\begin{aligned}
 R_x &= -is_x \tau_x \tilde{R}_x, \\
 R_y &= -is_y \sigma_x \tilde{R}_y, \quad (\text{A10})
 \end{aligned}$$

where \tilde{R}_i ($i = x, y$) represents the reflection operator for the envelop function with respect to axis i .

Actually, the terms proportional to σ_z (different on-site energies at A and B sites) [5] and $\tau_z \sigma_z s_z$ (the Kane-Mele term) [56] also commute with \mathcal{T} and C_3 , but V_{eff} lacks these terms due to the incommensurability between graphene and TMDC, as explained below. According to Eq. (6), the interlayer matrix element $\langle \tilde{\mathbf{k}}, X, \tilde{s} | H_{\text{int}} | \mathbf{k}, X, s \rangle$ occurs only when $\mathbf{k} + \mathbf{G} = \tilde{\mathbf{k}} + \tilde{\mathbf{G}}$. If the lattice structures of graphene and TMDC are incommensurate, there is at most only a single choice of $(\mathbf{G}, \tilde{\mathbf{G}})$ to connect specific pairs of \mathbf{k} and $\tilde{\mathbf{k}}$, because the primitive reciprocal vectors of graphene \mathbf{a}_i^* cannot be written in any linear combinations of those of TMDC $\tilde{\mathbf{a}}_i^*$'s. Then the difference in graphene's sublattice $X = A, B$ only matters in the global phase factor $e^{-i\mathbf{G} \cdot \tau_x}$ in Eq. (6), and it does not affect the diagonal terms of V_{eff} which are real numbers. Therefore we have the equal on-site energy at A and B for each spin-valley sector, so that the terms including σ_z are absent. When the system is commensurate, on the other hand, the interlayer hopping from \mathbf{k} to $\tilde{\mathbf{k}}$ is contributed by several paths with different \mathbf{G} 's, where the different phase factors $e^{-i\mathbf{G} \cdot \tau_x}$ interfere, leading to the sublattice dependence.

- [1] A. K. Geim and I. V. Grigorieva, *Nature (London)* **499**, 419 (2013).
- [2] A. Avsar, J. Y. Tan, T. Taychatanapat, J. Balakrishnan, G. Koon, Y. Yeo, J. Lahiri, A. Carvalho, A. Rodin, E. O'Farrell *et al.*, *Nat. Commun.* **5**, 4875 (2014).
- [3] T. Kaloni, L. Kou, T. Frauenheim, and U. Schwingenschlögl, *Appl. Phys. Lett.* **105**, 233112 (2014).
- [4] M. Gmitra and J. Fabian, *Phys. Rev. B* **92**, 155403 (2015).
- [5] Z. Wang, D.-K. Ki, H. Chen, H. Berger, A. H. MacDonald, and A. F. Morpurgo, *Nat. Commun.* **6**, 8339 (2015).
- [6] A. W. Cummings, J. H. Garcia, J. Fabian, and S. Roche, *Phys. Rev. Lett.* **119**, 206601 (2017).
- [7] T. S. Ghiasi, J. Ingla-Aynés, A. A. Kaverzin, and B. J. van Wees, *Nano Lett.* **17**, 7528 (2017).
- [8] S. Zihlmann, A. W. Cummings, J. H. Garcia, M. Kedves, K. Watanabe, T. Taniguchi, C. Schönenberger, and P. Makk, *Phys. Rev. B* **97**, 075434 (2018).
- [9] L. Antonio Benítez, J. F. Sierra, W. Saverio Torres, A. Arrighi, F. Bonell, M. V. Costache, and S. O. Valenzuela, *Nat. Phys.* **14**, 303 (2018).
- [10] T. Wakamura, F. Reale, P. Palczynski, S. Guéron, C. Mattevi, and H. Bouchiat, *Phys. Rev. Lett.* **120**, 106802 (2018).
- [11] J. H. Garcia, M. Vila, A. W. Cummings, and S. Roche, *Chem. Soc. Rev.* **47**, 3359 (2018).
- [12] T. Cysne, *Phys. Rev. B* **98**, 045407 (2018).
- [13] S. Carr, D. Massatt, S. Fang, P. Cazeaux, M. Luskin, and E. Kaxiras, *Phys. Rev. B* **95**, 075420 (2017).
- [14] R. Ribeiro-Palau, C. Zhang, K. Watanabe, T. Taniguchi, J. Hone, and C. R. Dean, *Science* **361**, 690 (2018).
- [15] M. Kindermann, B. Uchoa, and D. L. Miller, *Phys. Rev. B* **86**, 115415 (2012).
- [16] J. R. Wallbank, A. A. Patel, M. Mucha-Kruczyński, A. K. Geim, and V. I. Fal'ko, *Phys. Rev. B* **87**, 245408 (2013).
- [17] M. Mucha-Kruczyński, J. R. Wallbank, and V. I. Fal'ko, *Phys. Rev. B* **88**, 205418 (2013).
- [18] J. Jung, A. Raoux, Z. Qiao, and A. H. MacDonald, *Phys. Rev. B* **89**, 205414 (2014).
- [19] P. Moon and M. Koshino, *Phys. Rev. B* **90**, 155406 (2014).
- [20] C. Dean, L. Wang, P. Maher, C. Forsythe, F. Ghahari, Y. Gao, J. Katoch, M. Ishigami, P. Moon, M. Koshino, T. Taniguchi, K. Watanabe, K. Shepard, J. Hone, and P. Kim, *Nature (London)* **497**, 598 (2013).
- [21] L. A. Ponomarenko, R. V. Gorbachev, G. L. Yu, D. C. Elias, R. Jalil, A. A. Patel, A. Mishchenko, A. S. Mayorov, C. R. Woods, J. R. Wallbank, M. Mucha-Kruczynski, B. A. Piot, M. Potemski, I. V. Grigorieva, K. S. Novoselov, F. Guinea, V. I. Fal'ko, and A. K. Geim, *Nature (London)* **497**, 594 (2013).
- [22] B. Hunt, J. Sanchez-Yamagishi, A. Young, M. Yankowitz, B. LeRoy, K. Watanabe, T. Taniguchi, P. Moon, M. Koshino, P. Jarillo-Herrero, and R. Ashoori, *Science* **340**, 1427 (2013).
- [23] G. L. Yu, R. V. Gorbachev, J. S. Tu, A. V. Kretinin, Y. Cao, R. Jalil, F. Withers, L. A. Ponomarenko, B. A. Piot, M. Potemski, D. C. Elias, X. Chen, K. Watanabe, T. Taniguchi, I. V. Grigorieva, K. S. Novoselov, V. I. Fal'ko, A. K. Geim, and A. Mishchenko, *Nat. Phys.* **10**, 525 (2014).
- [24] J. M. B. Lopes dos Santos, N. M. R. Peres, and A. H. Castro Neto, *Phys. Rev. Lett.* **99**, 256802 (2007).
- [25] E. J. Mele, *Phys. Rev. B* **81**, 161405 (2010).
- [26] G. Trambly de Laissardiere, D. Mayou, and L. Magaud, *Nano Lett.* **10**, 804 (2010).
- [27] S. Shallcross, S. Sharma, E. Kandelaki, and O. A. Pankratov, *Phys. Rev. B* **81**, 165105 (2010).
- [28] E. Suarez Morell, J. D. Correa, P. Vargas, M. Pacheco, and Z. Barticevic, *Phys. Rev. B* **82**, 121407 (2010).
- [29] R. Bistritzer and A. H. MacDonald, *Proc. Natl. Acad. Sci. USA* **108**, 12233 (2011).
- [30] P. Moon and M. Koshino, *Phys. Rev. B* **85**, 195458 (2012).
- [31] G. Trambly de Laissardiere, D. Mayou, and L. Magaud, *Phys. Rev. B* **86**, 125413 (2012).
- [32] Y. Cao, V. Fatemi, S. Fang, K. Watanabe, T. Taniguchi, E. Kaxiras, and P. Jarillo-Herrero, *Nature (London)* **556**, 43 (2018).
- [33] Y. Cao, V. Fatemi, A. Demir, S. Fang, S. L. Tomarken, J. Y. Luo, J. D. Sanchez-Yamagishi, K. Watanabe, T. Taniguchi, E. Kaxiras, R. C. Ashoori, and P. Jarillo-Herrero, *Nature (London)* **556**, 80 (2018).
- [34] Z. Wang, Q. Chen, and J. Wang, *J. Phys. Chem. C* **119**, 4752 (2015).
- [35] D. Di Felice, E. Abad, C. González, A. Smogunov, and Y. Dappe, *J. Phys. D* **50**, 17LT02 (2017).
- [36] S. Hou, L. Han, L. Wu, R. Quhe, and P. Lu, *RSC Adv.* **7**, 45896 (2017).
- [37] W. Jin, P.-C. Yeh, N. Zaki, D. Chenet, G. Arefe, Y. Hao, A. Sala, T. O. Mentès, J. I. Dadap, A. Locatelli *et al.*, *Phys. Rev. B* **92**, 201409 (2015).
- [38] D. Pierucci, H. Henck, J. Avila, A. Balan, C. H. Naylor, G. Patriarche, Y. J. Dappe, M. G. Silly, F. Sirotti, A. C. Johnson *et al.*, *Nano Lett.* **16**, 4054 (2016).
- [39] L. Du and H. Yu, *Appl. Phys. Lett.* **111**, 263106 (2017).
- [40] C.-I. Lu, C. J. Butler, J.-K. Huang, Y.-H. Chu, H.-H. Yang, C.-M. Wei, L.-J. Li, and M.-T. Lin, *npj 2D Mater. Appl.* **1**, 24 (2017).
- [41] K. Song, D. Soriano, A. W. Cummings, R. Robles, P. Ordejón, and S. Roche, *Nano Lett.* **18**, 2033 (2018).
- [42] S. Fang, R. Kuate Defo, S. N. Shirodkar, S. Lieu, G. A. Tritsarlis, and E. Kaxiras, *Phys. Rev. B* **92**, 205108 (2015).
- [43] Y. Ma, Y. Dai, W. Wei, C. Niu, L. Yu, and B. Huang, *J. Phys. Chem. C* **115**, 20237 (2011).
- [44] S. Agnoli, A. Ambrosetti, T. O. Mentès, A. Sala, A. Locatelli, P. L. Silvestrelli, M. Cattelan, S. Eichfeld, D. D. Deng, J. A. Robinson, J. Avila, C. Chen, and M. C. Asensio, *ACS Appl. Nano Mater.* **1**, 1131 (2018).
- [45] M. Koshino, *New J. Phys.* **17**, 015014 (2015).
- [46] T. Ando, *J. Phys. Soc. Jpn.* **74**, 777 (2005).
- [47] A. H. Castro Neto, F. Guinea, N. M. R. Peres, K. S. Novoselov, and A. K. Geim, *Rev. Mod. Phys.* **81**, 109 (2009).
- [48] J. C. Slater and G. F. Koster, *Phys. Rev.* **94**, 1498 (1954).
- [49] T. Nakanishi and T. Ando, *J. Phys. Soc. Jpn.* **70**, 1647 (2001).
- [50] S. Uryu, *Phys. Rev. B* **69**, 075402 (2004).
- [51] W. A. Harrison, *Elementary Electronic Structure: Revised* (World Scientific, Singapore, 2004).
- [52] J. Huheey and T. Cottrell, *The Strengths of Chemical Bonds* (Butterworths, London, 1958).
- [53] W. S. Jenks, W. Lee, and D. Shuttters, *J. Phys. Chem.* **98**, 2282 (1994).
- [54] T. C. W. Mak, Z. Kristallogr. Cryst. Mater. **166**, 277 (1984).

- [55] E. Rudy, E. Rudy, and F. Benesovsky, *Monatsh. Chem.* **93**, 1176 (1962).
- [56] C. L. Kane and E. J. Mele, *Phys. Rev. Lett.* **95**, 226801 (2005).
- [57] E. McCann, *Phys. Rev. B* **74**, 161403 (2006).
- [58] E. McCann and M. Koshino, *Rep. Prog. Phys.* **76**, 056503 (2013).
- [59] P. Giannozzi, S. Baroni, N. Bonini, M. Calandra, R. Car, C. Cavazzoni, D. Ceresoli, G. L. Chiarotti, M. Cococcioni, I. Dabo *et al.*, *J. Phys.: Condens. Matter* **21**, 395502 (2009).
- [60] P. Giannozzi, O. Andreussi, T. Brumme, O. Bunau, M. B. Nardelli, M. Calandra, R. Car, C. Cavazzoni, D. Ceresoli, M. Cococcioni *et al.*, *J. Phys.: Condens. Matter* **29**, 465901 (2017).
- [61] J. P. Perdew, K. Burke, and M. Ernzerhof, *Phys. Rev. Lett.* **77**, 3865 (1996).
- [62] F. Guinea, *New J. Phys.* **12**, 083063 (2010).